Natural Resources Canada | Ressources naturelles Canada

GEOLOGICAL SURVEY OF CANADA
OPEN FILE 8097

Seismic stratigraphy of the Paleozoic succession and subsurface mapping of the Macasty Formation in Jupiter River area, Anticosti Island, Quebec, Canada

M.J. Duchesne, N. Pinet, V.I. Brake and D. Lavoie

2016

Canada

GEOLOGICAL SURVEY OF CANADA
OPEN FILE 8097

Seismic stratigraphy of the Paleozoic succession and subsurface mapping of the Macasty Formation in Jupiter River area, Anticosti Island, Quebec, Canada

M.J. Duchesne[1], N. Pinet[1], V.I. Brake[1] and D. Lavoie[1]

[1] Geological Survey of Canada -Quebec City, Quebec

2016

doi:10.4095/298895

This publication is available for free download through GEOSCAN (http://geoscan.nrcan.gc.ca/).

Recommended citation

Duchesne, M.J., Pinet, N., Brake, V.I., and Lavoie, D. 2016. Seismic stratigraphy of the Paleozoic succession and subsurface mapping of the Macasty Formation in Jupiter River area, Anticosti Island, Quebec, Canada; Geological Survey of Canada, Open File 8097, 31 p. doi:10.4095/298895

Publications in this series have not been edited; they are released as submitted by the author.

ABSTRACT

This study presents the methodology used for the processing and interpretation of seismic reflection data in the Jupiter River area of the Anticosti Island. The seismic characteristics of the rock formations investigated are described and time-structure maps of the tops of the Mingan and Macasty formations are presented as well as a map documenting the thickness variation of the Macasty Formation. Subsurface maps present time and thickness estimations that take into account exploration wells and regional seismic data, yet are limited by the spatial distribution and vertical resolution of seismic data. Time-structure maps of the top Mingan and Macasty formations portray a shallow and a deep domain delimited by the Jupiter Fault which probably corresponds to a composite structure with several ‘en échelon’ fault segments. The thickness map of the Macasty Formation reveals thicker accumulation and/or preservation of this unit within a NW-SE fairway bounded to the northeast by the Jupiter Fault and to the southwest by the Ruisseau Jean IV and the Rivière du Brick faults. North of the Jupiter Fault the Macasty Formation is considerably thinner.

RÉSUMÉ

Cette étude détaille la méthodologie utilisée pour le traitement et l'interprétation de données de sismique-réflexion dans le secteur de la rivière Jupiter sur l'île d'Anticosti. Les caractéristiques sismiques des formations rocheuses de cette région sont décrites et les cartes de la structure en temps du toit des formations de Mingan et de Macasty ainsi que la carte d'épaisseur de cette dernière formation sont présentées. Les estimations en temps et en épaisseur des cartes de sous-surface prennent en comptes les données sismiques et de forage, mais présentent néanmoins une incertitude liée à la distribution spatiale et la limite de résolution verticale des données sismiques. Les cartes de la structure en temps du toit des formations de Mingan et de Macasty documentent un domaine peu profond et un domaine profond délimités par la faille de Jupiter qui correspond probablement à une structure composite incluant plusieurs segments de failles en-échelon. Enfin, la carte d'épaisseur de la Formation de Macasty image une bande orientée NO-SE comprise entre la faille de Jupiter au nord-est et par les failles du Ruisseau Jean IV et de la Rivière du Brick au sud-ouest, où une plus grande épaisseur de sédiments de la Formation de Macasty ont été accumulés et/ou préservés. Au nord de la faille de Jupiter, la Formation de Macasty est considérablement plus mince.

INTRODUCTION

The Geological Survey of Canada's (GSC) first study of Anticosti Island was conducted in 1856 and resulted in the publication of detailed stratigraphic sections of the south shore from which a paleographical reconstruction was derived (Richardson, 1857). The shale of the Macasty Formation, which is now the primary target for hydrocarbon exploration, was first described by Sir William Logan in 1863 as rock fragments observed on beaches located at the northwest end of Anticosti Island (Schuchert and Twenhofel, 1910; Twenhofel, 1927). The onset of hydrocarbon exploration in the early 1960s led to single-fold seismic data acquisition and drilling mostly concentrated in the NW portion of the island. From the 1960s until the late 2000s exploration focused on the identification of conventional targets such as diagenetic and structural closures and fault-bounded hydrothermal dolomite reservoirs within the Upper Ordovician succession (Lavoie et al., 2009). Bertrand (1987) and Chen et al. (2016) identified the Macasty Formation as a good to excellent source rock due to its high organic matter content and thermal rank that suggest substantial oil, condensate and dry gas generation. Since 2010, the hydrocarbon industry has turned its attention towards unconventional oil and gas resource plays that generated a new interest in the Macasty Formation.

In 2014, the Geological Survey of Canada initiated 5 research activities related to unconventional resource exploration and development on Anticosti Island: 1) comparative fracture analyses between pre- and post-Taconian sedimentary successions from field and remote-sensing observations (Brake and Pinet, 2015; Pinet et al., 2015), 2) well-log geomechanical characterization of the Macasty Formation and overlying rocks (Séjourné, 2015a and 2015b), 3) seismic characterization of the Macasty Formation and its overlying sedimentary succession (Duchesne et al., 2016), 4) natural seismicity of Anticosti Island and 5) geological characteristics and unconventional in-place petroleum resource assessment of the Macasty Formation (Chen et al., 2016). This study is part of the third research activity and describes the methodology used for seismic processing and interpretation in the Jupiter River area. The interpretation was later used in the unconventional petroleum resource

assessment of Anticosti Island (Chen et al., 2016). The seismic characteristics of the rock formations encountered in the area are described as well as time-structure maps of the Mingan and Macasty formations, the thickness variation of the Macasty Formation and fault geometry.

GEOLOGICAL BACKGROUND

This study follows the standardized lithostratigraphy nomenclature of Bédard et al. (2014). However, as opposed to Bédard et al. (2014), the Ellis Bay and Becsie formations are kept separate from the Vauréal Formation since they can be identified on the seismic sections.

Anticosti Island is part of the large Anticosti Basin located in the northwestern portion of the Gulf of Saint Lawrence (Figure 1). The island consists of a gently dipping (~3^{o}) sedimentary succession thickening towards the southwest. The Anticosti Basin succession overlies the metamorphic rocks of the Precambrian Grenville domain. The base of the succession is formed by the 400-800 m thick assemblage of limestone and dolostone of the Lower Ordovician Romaine Formation (Figure 2; Desrochers et al., 2012). This formation is unconformably overlain by the 400-600 m thick carbonate-dominated Middle to Upper Ordovician Mingan Formation which is succeeded by the Upper Ordovician Macasty Formation (Desrochers, 1988). Although the Macasty is not exposed onshore, it has been encountered in all exploration wells drilled on the island with the exception of one well located on its eastern tip. The thickness of this shale-dominated and organic-rich interval varies from 0 to 125 m. The Macasty Formation is covered by the 900-1200 m thick Upper Ordovician Vauréal Formation. The Vauréal is subdivided into two units; the lower Vauréal consisting of a mudstone-dominated rock interval and the upper Vauréal, an interbedded limestone and limey-shale. The upper Vauréal is overlain by the ~60 m thick carbonates of the Upper Ordovician Ellis Bay Formation and the 400 m thick carbonate-dominated, lower Silurian Anticosti Group which includes the Becscie, Merrimack, Gun River, Jupiter and Chicotte formations (Achab et al., 2011; Desrochers, 2006; Desrochers et al., 2010; Sami and Desrochers, 1992).

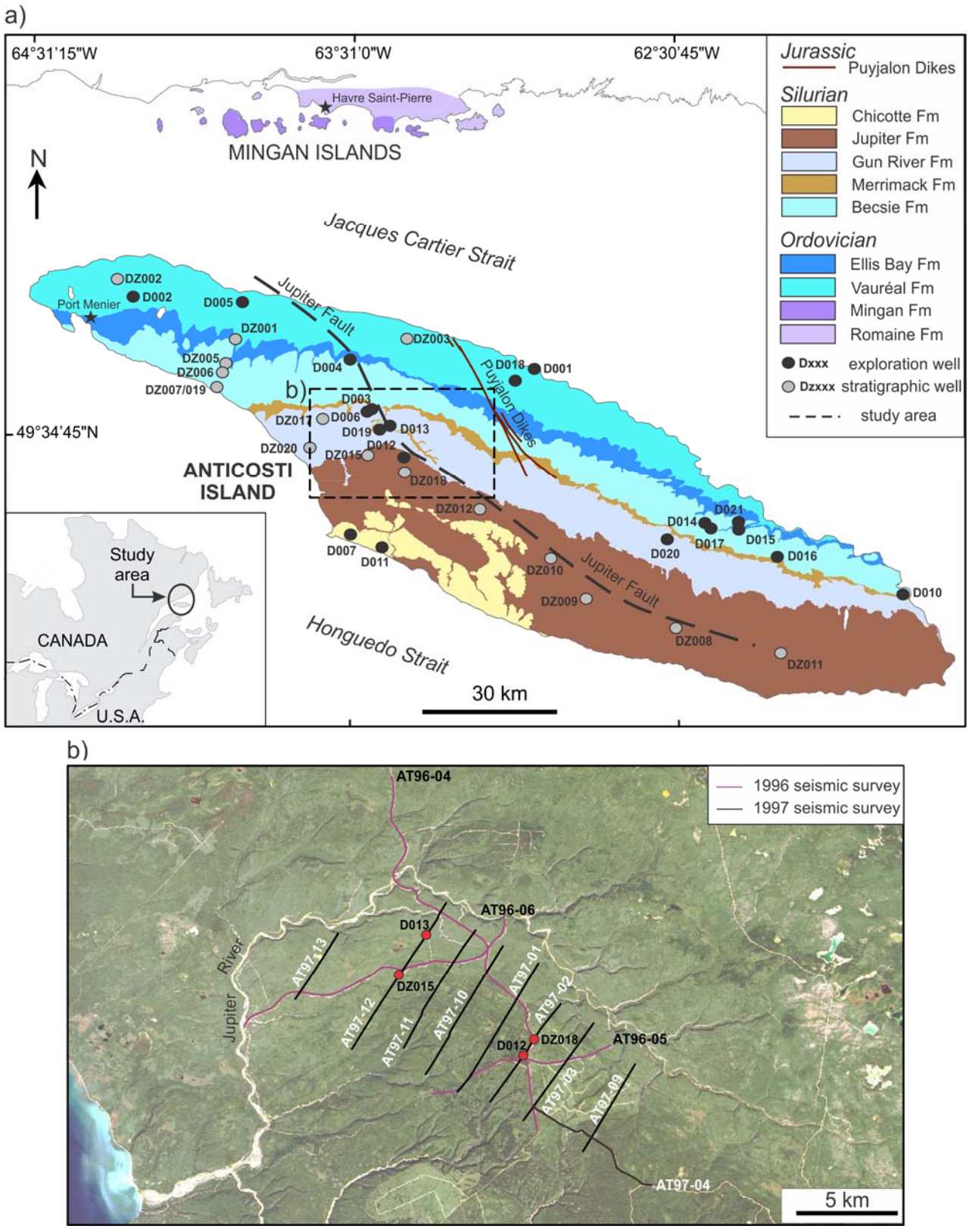

Figure 1. a) Geological map of Anticosti and Mingan islands with well locations. b) Satellite image of the study area with well and survey track line locations.

The outcropping sedimentary succession of Anticosti Island is weakly deformed and affected by minor faults and fracture networks that witness far field foreland strain related to the Appalachian orogenesis and younger events (Bordet et al., 2010; Pinet et al., 2015). Previous seismic interpretation also revealed that the base of the sedimentary succession, up to the base of the Vauréal Formation is cut by several high-angle faults, the greatest throws being associated with the Jupiter Fault (Figure 1; Lynch, 2001; Castonguay et al., 2005; Bordet et al., 2010). Finally, a thickening of the sedimentary succession in the hanging wall of the Jupiter Fault is observed as depth-to-basement passes from 2153 m in well D013 to 3828 m in well D007 that are respectively located 1.5 km north and 21 km south of the fault (Figure 1).

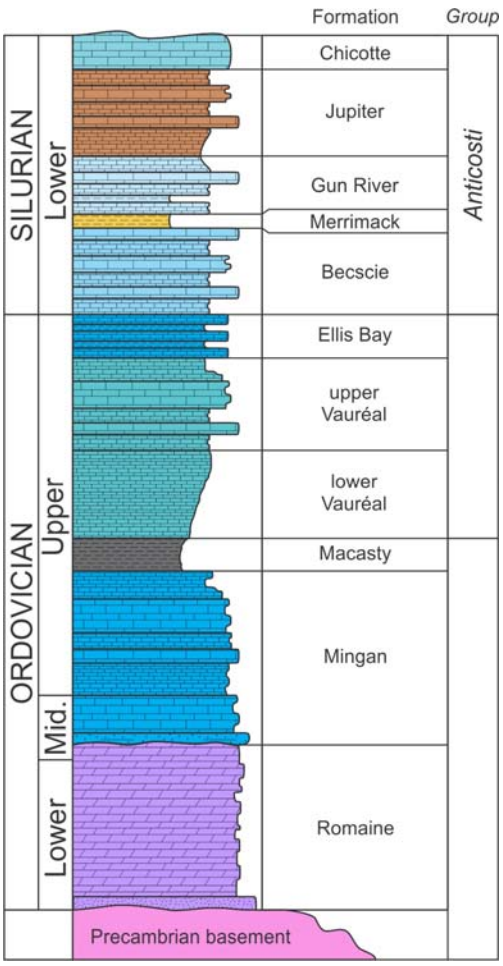

Figure 2. Stratigraphic column of the Silurian-Ordovician Anticosti basin (modified from Bédard et al., 2014).

DATASETS

This research activity relied on an unrestricted data access agreement for stacked seismic data with 'Hydrocarbures Anticosti', a limited partnership between Ressources Québec, Pétrolia, Corridor Resources and Saint-Aubin E&P. The Ministère de l'énergie et des ressources naturelles du Québec also provided access to all public well-log data and the 2014-2015 stratigraphic well program of 'Hydrocarbures Anticosti'.

Seismic data

Two 2-D seismic reflection data acquisition programs were conducted in 1996 and 1997 in the Jupiter River area (Figure 1). In this study 12 lines (i.e 3 from 1996 and 9 from 1997) for a total of 105 linear-km were reprocessed and interpreted. Line spacing is variable ranging from 3.7 to 1.6 km with an average spacing of ~2 km. The 1996 program was collected with one dynamite charge of 1 kg per shot point with a spacing of 64 m. The receiving system consisted of a 3056 m long spread with a receiver station deployed every 16 m. The program that was shot in 1997 used a slightly different acquisition geometry as 1 kg dynamite charges were fired every 60 m along a 2880 m long spread with receivers deployed at a 20 m interval. Acquisition fold was 2400% for both programs whereas sampling rate was set to 2 ms in 1996 and 1 ms in 1997. Overall, data quality is good to very good with the 1997 data set having the highest quality. The reason for this is mostly attributed to the larger number of receivers deployed per station in 1997 (9 over 20 m) versus 1996 (6 over 16 m) from which a higher signal-to-noise ratio can be reached.

Well data

For this study four types of well logs from four locations (Figure 1) were used: sonic, density, gamma-ray and caliper. Sonic logs were used to build time-depth charts, so that well information could be converted from the depth to time domain in order to be projected onto seismic lines. The sonic logs were also used along with density logs to generate 1-D synthetic seismograms. Gamma-ray curves served as a correlation tool to ensure that formation tops were correctly positioned. Finally, the

caliper log helped to verify well wall integrity and identified spurious values on the other three log types that were later edited.

METHODOLOGY

Seismic processing

Pre-stack processing was carried out by Geo-X Exploration Services. The pre-stack processing flow included surface consistent deconvolution, structure and surface static corrections, velocity analysis followed by normal moveout corrections, surface consistent residual static, common-midpoint (CMP) cross-correlation statics and weighted cross-correlation CMP stacking.

Post-stack reprocessing was conducted by the GSC using stack sections generated by Geo-X Exploration Services. One goal of the reprocessing was to provide greater resolution at depth in order to have a better control on the thickness of the Macasty Formation in support of its petroleum resource assessment (Chen et al., 2016). Reprocessing targeted the coherent and incoherent noise that plagued the stacked data. Coherent noise corresponded to residual dynamite shot noise. This type of noise was removed in the time-distance domain (T-X) where noise wavelets were constructed along the dips of the dynamite shot noise by including all frequencies contained in the bandwidth of this noise. Modelled wavelets were matched for statics and amplitude with their corresponding trace on the 2-D section so that wavelets were not smeared by static jumps or noise curvature. Dips were calculated using linear moveout (LMO) velocities and each dip was processed separately. Finally, modelled noise wavetrains were adaptively subtracted from the original stacked data. Random noise was isolated Principal Component Decomposition (i.e. Karhunen-Loève transform; Jones and Levy, 1987) before being subtracted from the data. Next, data were migrated using the phase-shift plus interpolation (PSPI) method of Gazdag and Sguazzero (1984). The PSPI method was chosen due to its ability to handle lateral velocity variations. Thus, it was capable of coping with the widely spaced CMP velocity analysis (on average 1 analysis per 40 CMPs) provided by the initial pre-stack processing (Figure 3).

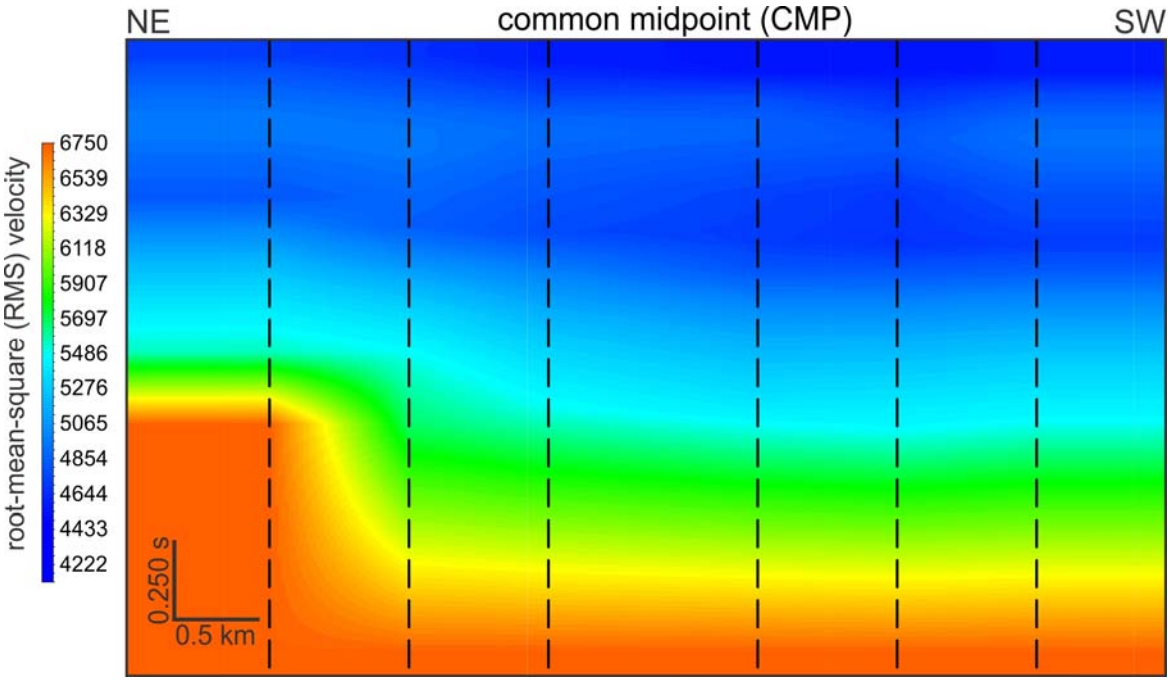

Figure 3. Interpolated RMS velocity model used for migrating line AT97-02. Dashed lines locate the CMPs on which velocity analyses have been conducted.

PSPI migration can accommodate lateral velocity variations using a two-step approach: (1) the wave field is extrapolated by using the second-order approximation to the 2-D scalar wave equation written in a downward-moving source and receiving coordinate system, (2) the subsequent wave field is interpolated from reference velocity fields. For all seismic lines, 5 reference velocity fields were used so that the geometric progression of the downward-moving coordinate system is smooth in order to avoid seismic imaging distortions. Finally, high-frequency components of the migration noise were separated from the signal with a prediction filter before a band-pass filter (5/20-125/165Hz) was applied to enhance the energy across the bandwidth of interest (Figure 4). The application of the post-stack reprocessing strategy has increased the signal-to-noise ratio from an average of 1.1 on the original stack sections to an average 5.6 on the reprocessed sections.

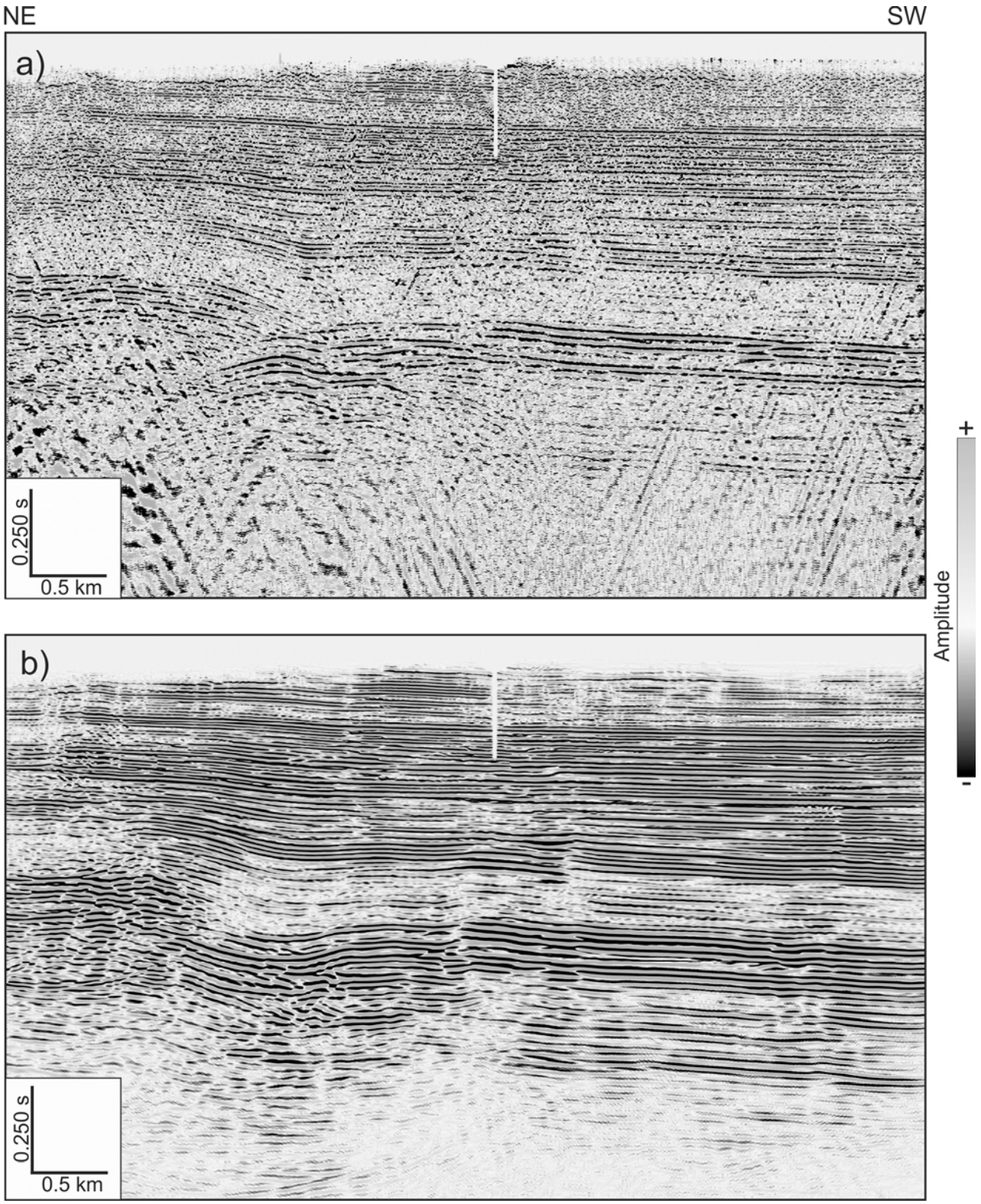

Figure 4. a) Original stack of line AT97-02 used for reprocessing and b) line AT97-02 after the application of the post-stack processing flow.

Seismic-to-well ties

For each well a time-depth chart was generated from sonic logs which are a measure of slowness, the reciprocal of velocity. Hence, instantaneous velocity (V_{inst}) was first obtained directly from sonic logs from

$$V_{inst} = \frac{1}{DT} \tag{1}$$

where *DT* is the delta transit-time or sonic value at a given depth. Then, the interval velocity (V_{int}) was calculated for each formation following

$$V_{int} = \frac{\sum z_i}{\sum t_i} \tag{2}$$

where z_i is the measured depth at each sampling point of the well log and t_i is the one-way time at each sampling point obtained from

$$t_i = \frac{z_i}{V_{inst}} \ . \tag{3}$$

Next, the time interval (t_{int}) of each formation is computed from

$$t_{int} = \frac{z_i}{(\frac{V_{int}}{2})} \tag{4}$$

before all time intervals are summed and adjusted to the time datum of the seismic line.

Afterward, synthetic seismograms were used to tie well information to the seismic data (Figure 5). Synthetic seismograms were produced from the computation of a reflection coefficient series obtained by the product of instantaneous velocity and density, two properties available in well logs, convolved with a seismic wavelet (Sheriff and Geldart, 1995). In this study stationary zero-phase seismic wavelets were modeled using the average of the frequency spectra extracted from 50 traces of the seismic section centered on the well using the frequency matching method (Matheney and Nowack 1995).

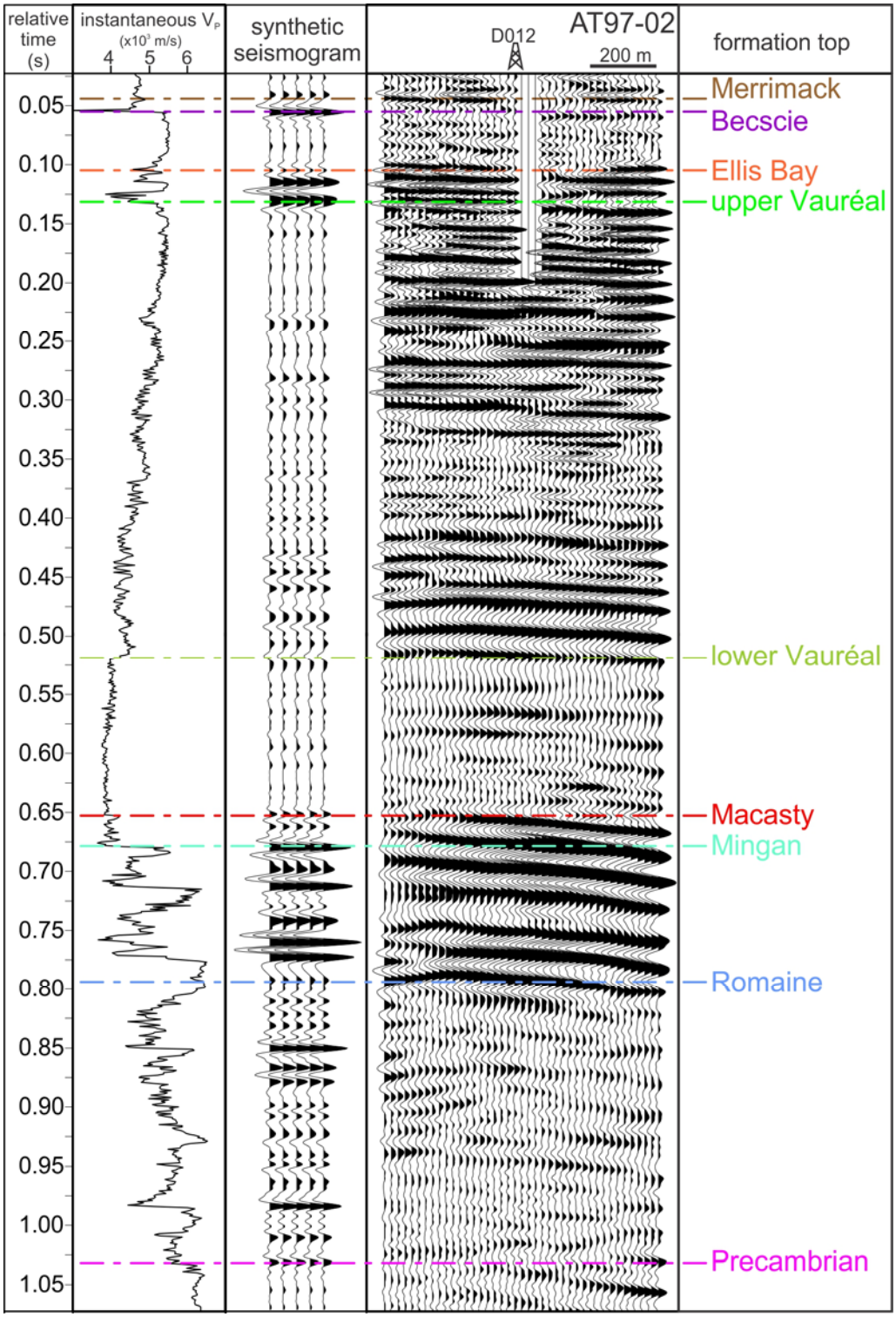

Figure 5. Seismic-to-well tie at well D012. From left to right: relative time-scale, instantaneous P-wave velocity log derived from slowness measurements, synthetic seismogram, mini-section extracted at well location and formation top picks. Note that time scale is relative to the first slowness value recorded on the wireline log.

Seismic interpretation

Seismic horizons and fault surfaces picking

Reflections or horizons corresponding to formation tops were picked laterally away from the wells using synthetic seismograms based on coherency and amplitude. Reflections were picked semi-automatically using a 0.020 s time gate and edited manually on the selected seismic sections. Seed points were generated where seismic traces on cross-lines overlap, permitting the horizons to be correlated to adjacent lines.

The location of faults and their throws were also interpreted on all seismic lines. Following the interpretation of faults on the 2-D seismic profiles, the faults were correlated between adjacent seismic lines based on the variation of throws from one line to the other and using several aeromagnetic images in Lynch (2001).

Subsurface Mapping

Three subsurface maps were generated from the picked horizons constrained by the fault interpretation: time-structure maps of the top Mingan and Macasty formations and a thickness map of the Macasty Formation. All maps were generated using a gradient projection optimization algorithm (GPOA) (Rosen, 1960 and 1961). This method is said to be data-adaptive because it computes X, Y and Z (i.e. time, depth or thickness) derivatives for every trace where the seismic horizon is picked to build a projection matrix, respecting variations that naturally occur within the data set. The optimization considers predetermined constraints such as the minimum and maximum X and Y distances and lower and higher limits of Z values encountered over the search area. Then, the optimization scheme uses the gradient (or slope) of tangent hyperplanes built from the original XYZ horizon coordinates. Finally, an inverse distance to a power weighting interpolation is employed to project values on the grid nodes. In this project, 9696 picks spread over an area of ~330 km^2 were used to generate each subsurface map using a cell size of 10x10 m. Small cell sizes were required for horizons and fault surfaces to be represented as accurately as possible (Figure 6).

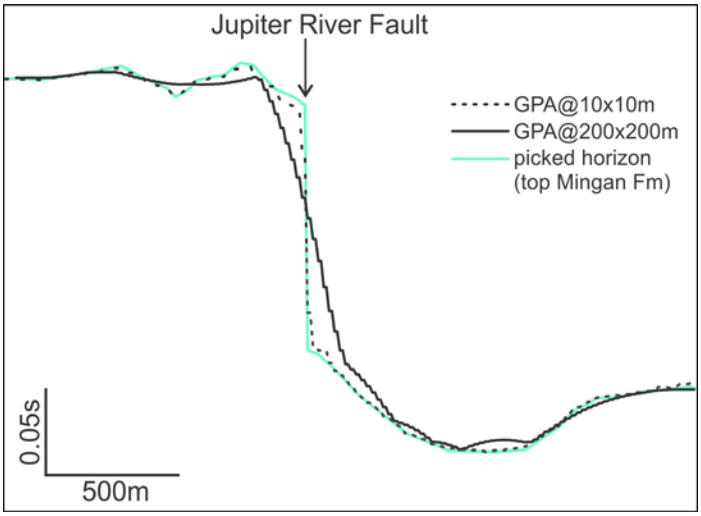

Figure 6. Comparisons between the accuracy of 200x200 m and 10x10 m cell sizes to model surfaces from the gradient projection optimization algorithm (GPOA).

The thickness map of the Macasty Formation was computed as follows. First, the time-interval (or t_{int}) of the formation was obtained from the subtraction between the horizon time picks of the Mingan and the Macasty formation tops. Then, root-mean-square velocities (V_{rms}) used for processing were converted to interval velocities using the method of Dix (1955):

$$V_{int} = \left[\frac{V_{rms_n}^2 t_n - V_{rms_{n-1}}^2 t_{n-1}}{t_n - t_{n-1}}\right]^{1/2} \quad (5)$$

where t is the time of the picked horizons. Finally, the thickness (z) is calculated from

$$z = V_{int}\,\frac{t_{int}}{2} \ . \quad (6)$$

RESULTS

Seismic stratigraphy

The deepest reflection that could be tied to well data was noted in wells D012 and D013 that are positioned on lines AT97-02 and AT97-12 respectively (Figure 1). It corresponds to a coherent flat lying low frequency reflection with amplitude laterally passing from high to low which represents the limit between the Precambrian rocks and the overlying Romaine Formation (Figure 7). Above that

contact, sits a coherent, parallel reflection package where seismic events can easily be followed although their amplitude may suddenly dim out or brighten laterally. The time-interval of the seismic package is greater southwest of the Jupiter Fault where it ranges from 0.247 to 0.280 s (average 0.264 s), whereas to the northeast this time-interval ranges from 0.119 to 0.166 s (average of 0.146 s). This interval correlates to the Romaine Formation. On top of this interval lays a series of highly reflective interfaces sharply bordered by high amplitude parallel reflections. The seismic unit ties to the Mingan Formation. The reflection at the base of the Mingan Formation is most likely induced by a ~10m thick high-velocity sandstone-dominated layer associated with the Sauk-Tippecanoe erosional unconformity, the commonly assumed transition between passive margin and orogenic foreland basin in North America (Sloss, 1963). The reflection at the top of the Mingan Formation is associated with an abrupt decrease in velocity corresponding to the passage from carbonates to shale (Desrochers et al., 2012). Internal reflections are typically of high amplitude and subparallel, correlative with alternating high and low velocity layers attributed to a gradual variation of the shale/limestone ratio (Bédard et al., 2014). Along the seismic lines, the Mingan Formation possesses a near constant time-interval regardless of its position to the Jupiter Fault, with measured interval times ranging between 0.129 and 0.161 s for an average value of 0.144 s. Gently draping above the Mingan Formation, is a short time-interval characterized by a low frequency medium to high amplitude reflection at its base and by a weak to medium thin amplitude reflection that lacks coherence at its top. This lack of coherence and the lateral change in amplitude mark the top of the Macasty Formation which is sometimes hard to pick in the Jupiter River area. The high amplitude reflection delimiting the bottom of the Macasty Formation is attributed to the large velocity (~1245 m/s) difference with the top of the Mingan Formation whereas the low amplitude reflection delineating its top is most likely due to the weak velocity (~485 m/s) contrast with the base of the Vauréal Formation. Across the study area, the time-interval of the Macasty ranges from 0.010 to 0.083 s with an average value of 0.038 s. The Macasty Formation is topped by an interval that can be subdivided in two units. The lower unit is

characterized by weak amplitude, continuous, low frequency reflections. Although, the reflections are of low amplitude they can be easily traced along the sections because of their high coherence. The upper unit possesses the same reflection configuration as the lower unit except that reflections are of high amplitude. The interval corresponds to the Vauréal Formation. The transition between the two units is marked by a sharp increase in velocity; i.e. ~3850 m/s to ~4350 m/s at the top of the lower Vauréal Formation. These reflections are correlative to several velocity variations within the unit that are, from well log interpretation, tied to alternations of limestone and limey-shale rock intervals. The Vauréal Formation has a nearly constant time-interval along all the lines with values ranging from 0.536 to 0.604 s for an average of 0.569 s. The upper Vauréal dominates the bulk of the time-interval with measured times extending between 0.382 and 0.456 s for an average of 0.423 s. Resting on the Vauréal Formation are medium to high amplitude and low frequency flat reflections. At wells D012 and D013, these reflections are characterized by a high velocity zone of ~5500 m/s bordered by two lower velocity intervals of ~4550 and ~4700 m/s at the bottom and top respectively. Both low velocity intervals are tied to higher neutron porosity values (Bédard et al., 2014). This time-interval representing the Ellis Bay Formation is constant, and ranging from 0.024 to 0.034 s with an average of 0.030 s. On top of this formation lays a weak to medium amplitude and subparallel reflection package marked by a continuous high velocity of ~5500 m/s. This unit has a relatively constant time-interval along the survey track lines that varies from 0.049 to 0.063 s for an average of 0.056 s correlating to the Becscie Formation. In the study area, this formation possesses a southward thinning trend of a few milliseconds. Over the Becscie Formation lies the shallowest marker that can be traced along the seismic lines. This marker is represented by a single discontinuous horizontal high amplitude reflection of ~0.010 s that sometime lacks coherence because of residual shot noise. The reflection is characterised by a gradual upward increase in velocity of ~4600 to ~4900 m/s which delimits the top of the Merrimack Formation. The seismic characteristics of the interval above are highly variable because of residual static effects and shot noise in the data but flat lying reflections are occasionally

imaged. The time-interval of this formation is hard to approximate because of topographic variations and the absence of a clear marker at its top. Based on well information the interval represents the strata of the Gun River Formation.

Faults

Three main faults are interpreted; the NW-striking Jupiter Fault zone, that crosses the entire study area, the (new) Ruisseau Jean IV Fault at the NW and (new) Rivière du Brick Fault at the SE that are both grossly parallel to the Jupiter Fault. The Jupiter Fault zone is observed on all lines except line AT97-13 and is marked by sharp changes in the reflection time for all seismic markers from the top of the Precambrian up to the top of the Macasty Formation/lowermost part of the Vauréal Formation (Figure 7). On Figures 8 to 10, the fault is traced as a single structural feature to facilitate time-structure map computation. However, in the study area, the Jupiter Fault zone includes three 'en échelon' segments. Each segment exhibits variable normal motions, with smaller throws at their tips. The maximum throw observed along seismic lines is 0.149 s. The detailed fault zone geometry in the area where fault segments partly overlap in map view is not well constrained by the data and it is presently unknown if the main fault segments form soft-linked relay zones or are partly connected by secondary order structures (breached relay zone). In extensional settings, such transfer zones between two fault segments are frequently characterized by rock unit thickness variations, higher fracture density and subtle change in the dip of bedding (Giba et al., 2012; Rotevatn and Bastesen, 2014; Fossen and Rotevatn, 2016). Such specific characteristics of relay zones are not captured in the time-structure maps presented below, and the interpretation in zones characterized by a change in strike of the fault (simplified geometry of relay zone) should be envisioned with caution.

Two NW-striking, NE-dipping faults are located ~ 2 km to the SW of the Jupiter Fault zone. Despite their subparallel traces, the possibility that they form a single structure is unlikely as no faults with throw > 0.01 s were present on line AT97-10 southwest of the Jupiter Fault zone.

The Ruisseau Jean IV Fault is observed on lines AT97-12, AT96-6 and AT97-11. This fault exhibits a maximum throw of ~0.36 s and affects seismic markers of the Precambrian up to the Macasty Formation. The presence of several relatively small (<0.2 s) throw faults on line AT97-11 suggests that the SE end of the fault may be characterized by a horsetail geometry. The Rivière du Brick Fault is identified on lines AT97-01, AT97-02, AT96-04, AT96-5 and AT97-03 and exhibits a maximum throw of 0.054 s. Its interpretation on line AT96-05 may capture a change in direction as the fault trace may pass from NW-SE to NNW-SSE.

Subsurface maps

Figures 8, 9 and 10 show time-structure maps of the top of Mingan and Macasty formations and thickness map of the Macasty Formation in the Jupiter River area. On all three maps, survey track lines are displayed to assess the uncertainty and the effect of the survey grid on maps computation. Histograms of formation top picks are also provided for each map so the statistical weight of the values used to compute the maps can be pondered. Time-interval and interval velocity maps of the Macasty Formation used to calculate the thickness map presented on Figure 10 are presented in appendixes 1 and 2.

Time-structure maps of the top Mingan and Macasty formations show similar features (figures 8 and 9): 1) they image two domains delimited by the Jupiter Fault zone, 2) greater two-way travel times south of the Jupiter Fault zone between lines A97-13 and AT96-6, 3) histograms present two two-way travel time populations that are correlative with the reflections picked north and south of the Jupiter Fault zone and 4) as noted above, in some locations close to relay zones associated with segments of the Jupiter Fault zone, the GPOA may be less accurate.

The thickness map of the Macasty Formation was generated without using interval velocities computed along lines AT96-4 and AT97-4 grossly oriented NW-SE, therefore parallel to the Jupiter Fault, because of suspected azimuthal seismic anisotropy documented by velocity function misties located at the intersections of the seismic lines (Williams and Jenner, 2002). The map reveals thicker

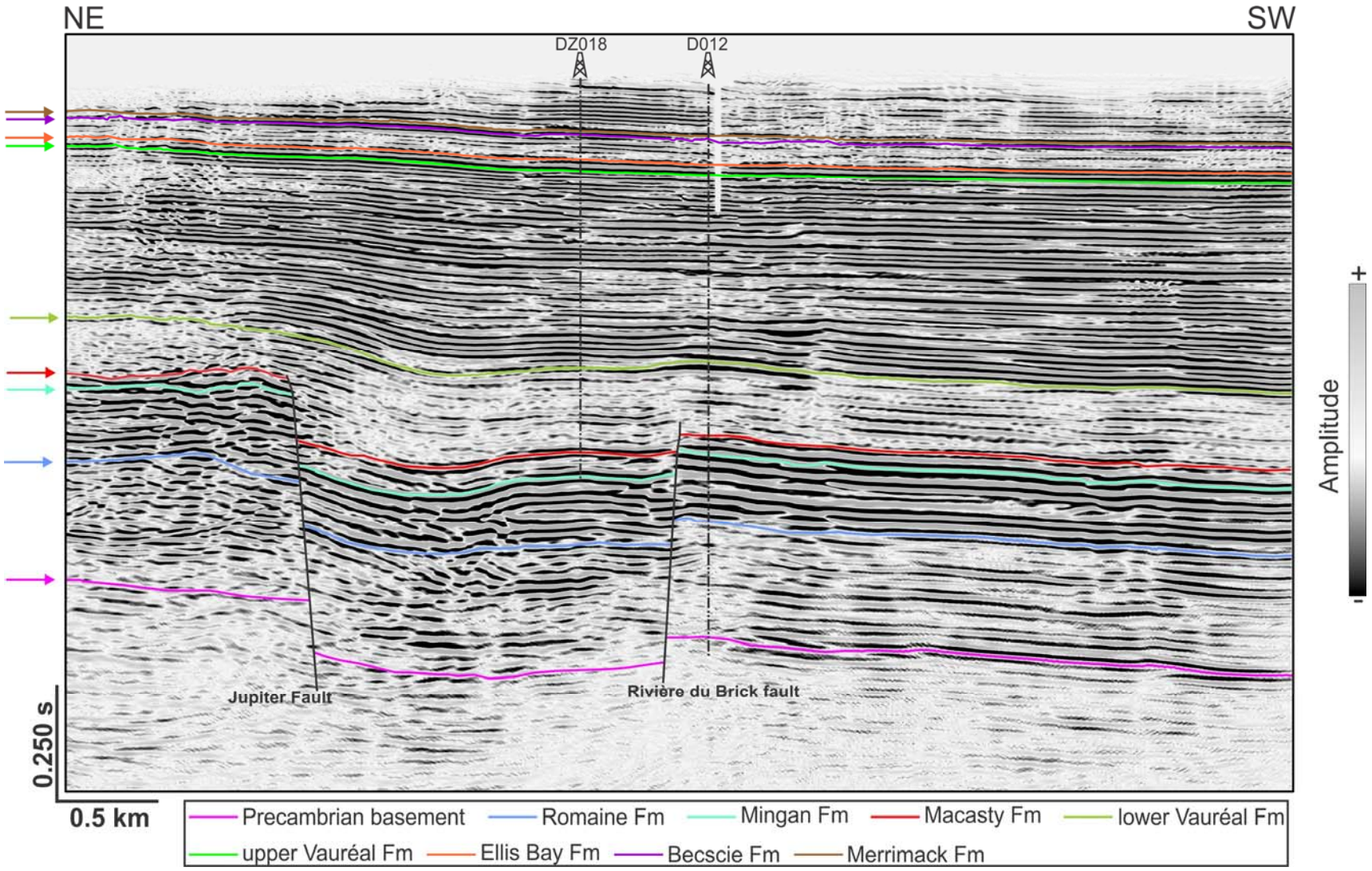

Figure 7. Seismic interpretation of line AT97-02. See Figure 1b for line and well locations.

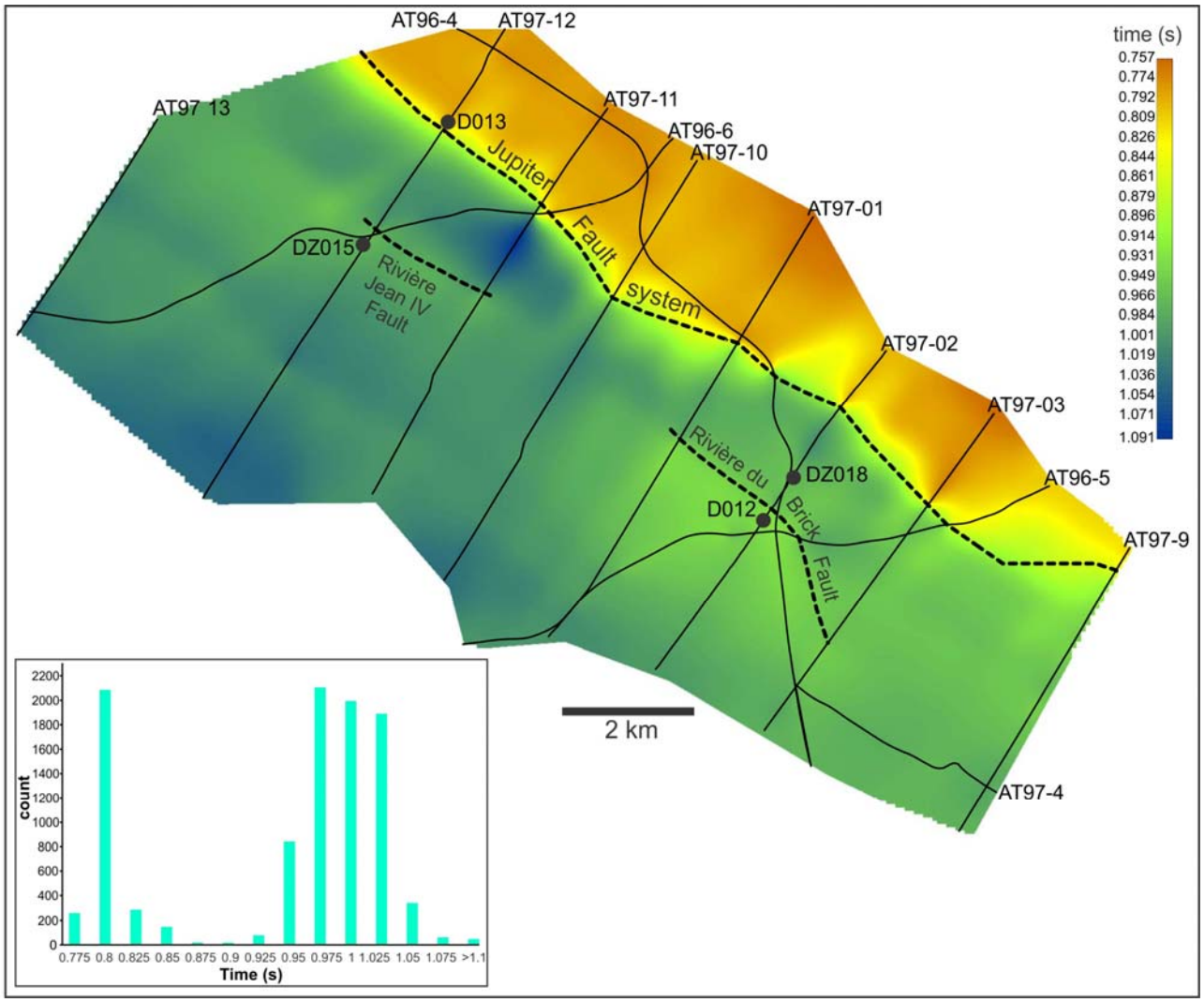

Figure 8. Time-structure map of the top Mingan Formation computed with the gradient projection optimization algorithm (GPOA). Inset shows the distribution of the time picks. Fault traces used for map generation are simplified in order to facilitate model generation. More complex segmented fault geometries are envisioned based on seismic interpretation.

accumulation and/or preservation of the Macasty within a NW-SE fairway delimited to the north by Jupiter Fault and to the south by the Ruisseau Jean IV and Rivière du Brick faults. North of the Jupiter Fault the Macasty Formation is considerably thinner. Thickness estimations obtained by equations (5) and (6) and mapped using the GPOA were ground truthed at 4 well sites (Figure 10 and Table 1). At

two of the four well locations (D012 and D013) the method overestimates the thickness of the Macasty Formation by 10 and 16 m. At wells DZ015 and DZ018, where the thickest occurrence of Macasty is encountered, the method underestimates the thickness by 10 m and 12 m respectively.

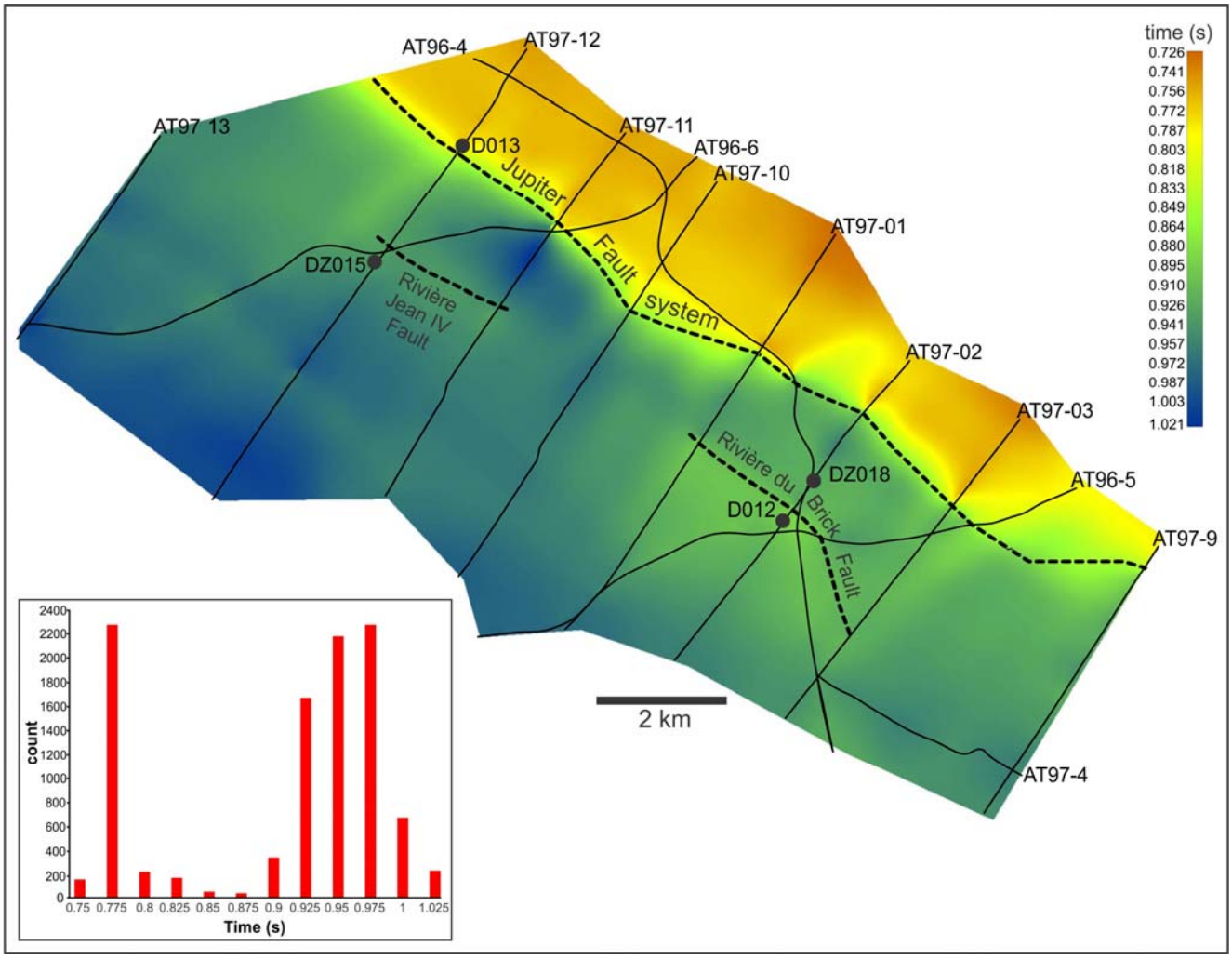

Figure 9. Time-structure map of the top Macasty Formation computed with the gradient projection optimization algorithm (GPOA). Inset shows the distribution of the time picks. Fault traces used for map generation are simplified in order to facilitate model generation. More complex segmented fault geometries are envisioned based on seismic interpretation.

Table 1. Comparisons between measured (from well logs) and estimated thicknesses of the Macasty Formation at well locations.

Well no.	Measured thickness in well (m)	Estimated thickness from seismic data (m)
D013	16	32
DZ015	87	77
DZ018	105	93
D012	59	69

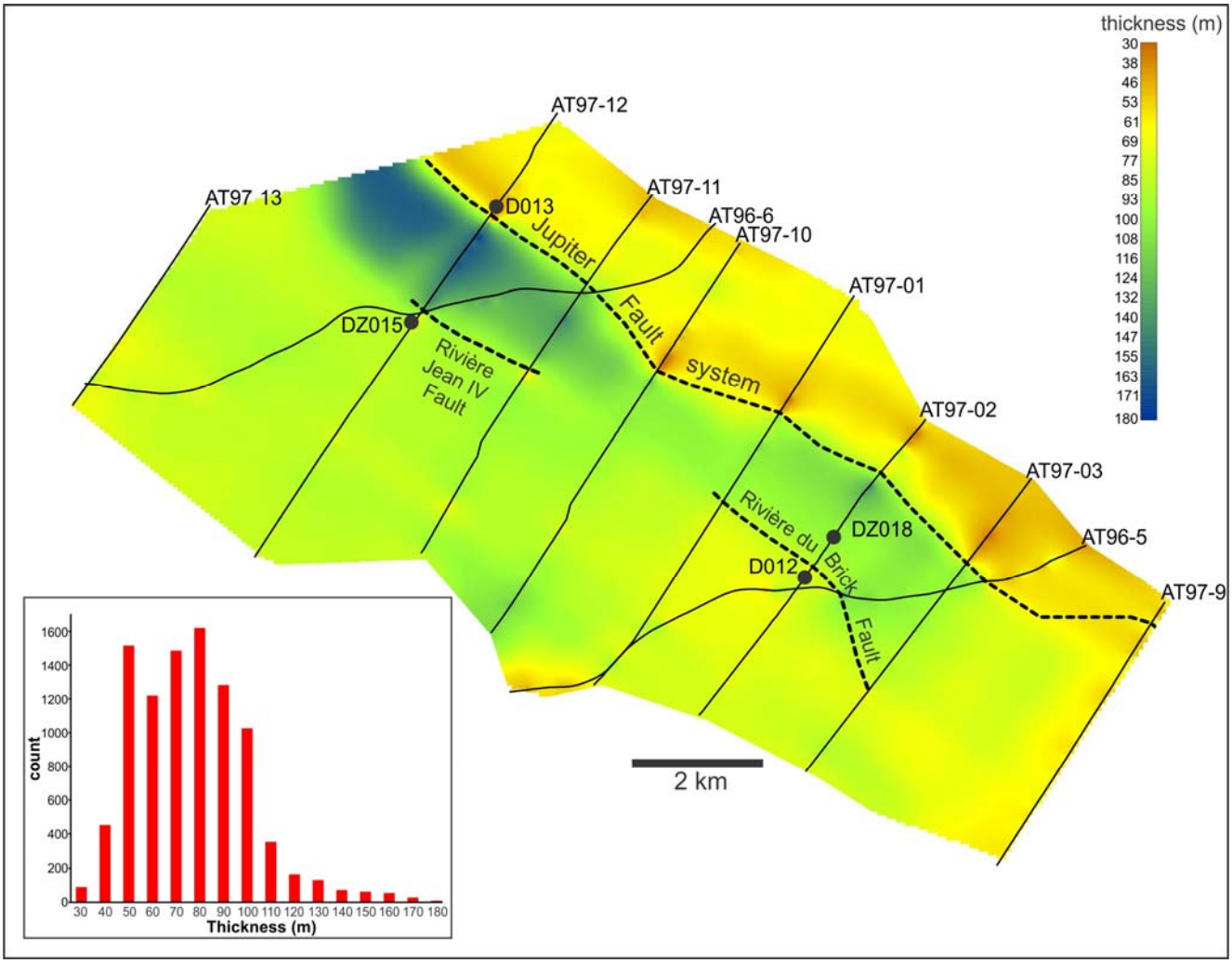

Figure 10. Thickness map of the Macasty Formation computed with the gradient projection optimization algorithm (GPOA). Inset shows the distribution of the thickness estimations. Fault traces used for map generation are simplified in order to facilitate model generation. More complex segmented fault geometries are envisioned based on seismic interpretation.

DISCUSSION

The reprocessing strategy has enhanced the subsurface imaging in the Jupiter River area by significantly increasing the signal-to-noise ratio and the vertical resolution of the seismic data. Overall the interpretation of the Paleozoic succession was improved; in particular the the Macasty Formation could be picked with greater confidence. Fault positioning remains difficult on some of the lines because of their suspected steepness and the post-stack migration that provides smoother but less accurate imaging than pre-stack migration. Moreover, the complexity of the fault network in map view is suspected but poorly constrained by seismic data. High-resolution aeromagnetic images (Lynch, 2001) tend to support the interpretation in which the Jupiter Fault, the most prominent fault in the area, includes several segments, but the detailed geometry of the fault network remains poorly defined. Minor faulting was also observed on the sections but is not reported here because it could not be followed on successive lines.

Spatial data distribution is highly anisotropic as time picks have a 20 m spacing along seismic lines, but are >1 km distant between lines. Wide line spacing was a hurdle to the propagation of the information through map computing between lines which also contribute to increase the uncertainty. The use of partial derivatives combined to small cell sizes within the GPOA helped to propagate errors following a mean squared method so uncertainty is minimized.

GPOA estimation is believed to capture the main trend of thickness variations of the Macasty Formation and differences with well measurements may be explain by the vertical resolution of the seismic data, which is ~ 9 m at the depth of the Macasty Formation and by the wide spacing of CMP velocity analysis from which interval velocities were derived.

CONCLUSION

This report describes the methodology used for seismic processing, subsurface interpretation and mapping in the Jupiter River area which resulted in an estimation of the thickness of the Macasty Formation that was later employed for its unconventional petroleum resource assessment (Chen et al., 2016). As part of the work, seismic characterisation of rock formations and faults encountered in the area was performed. Subsurface maps derived from seismic data allow the documentation of time-structure variations for the Mingan and the Macasty formations and thickness variations of the Macasty Formation over an area of ~330 km^2. Although uncertainty exists because of the spatial data distribution and vertical resolution limit of the seismic data, the method selected (i.e. gradient projection optimization algorithm) to generate the subsurface maps has produced time and thickness estimations that capture the main trend of the data.

AKNOWLEDGMENTS

Zhuoheng Chen of the GSC-Calgary is acknowledged for reviewing this report. Anticosti Hydrocarbons L.P. is thanked for data access. We are grateful to Paul Durling (Corridor Resources) for sharing his knowledge of the data set which was essential for its reprocessing. Martin Bêche (Pétrolia) is also acknowledged for his insight concerning the seismic characterization of the Macasty Formation. The Ministère de l'énergie et des ressources naturelles du Québec contributed to this research by providing us access to all public domain geoscience data. Finally, we would like to thank Karine Bédard and Félix-Antoine Comeau of the Institut National de la Recherche Scientifique, Centre Eau-Terre-Environnement for appreciated comments on their standardized lithostratigraphy nomenclature.

APPENDIX 1.

Time-interval map of the Macasty Formation computed with the gradient projection optimization algorithm (GPOA). Inset shows the distribution of the time-interval calculations.

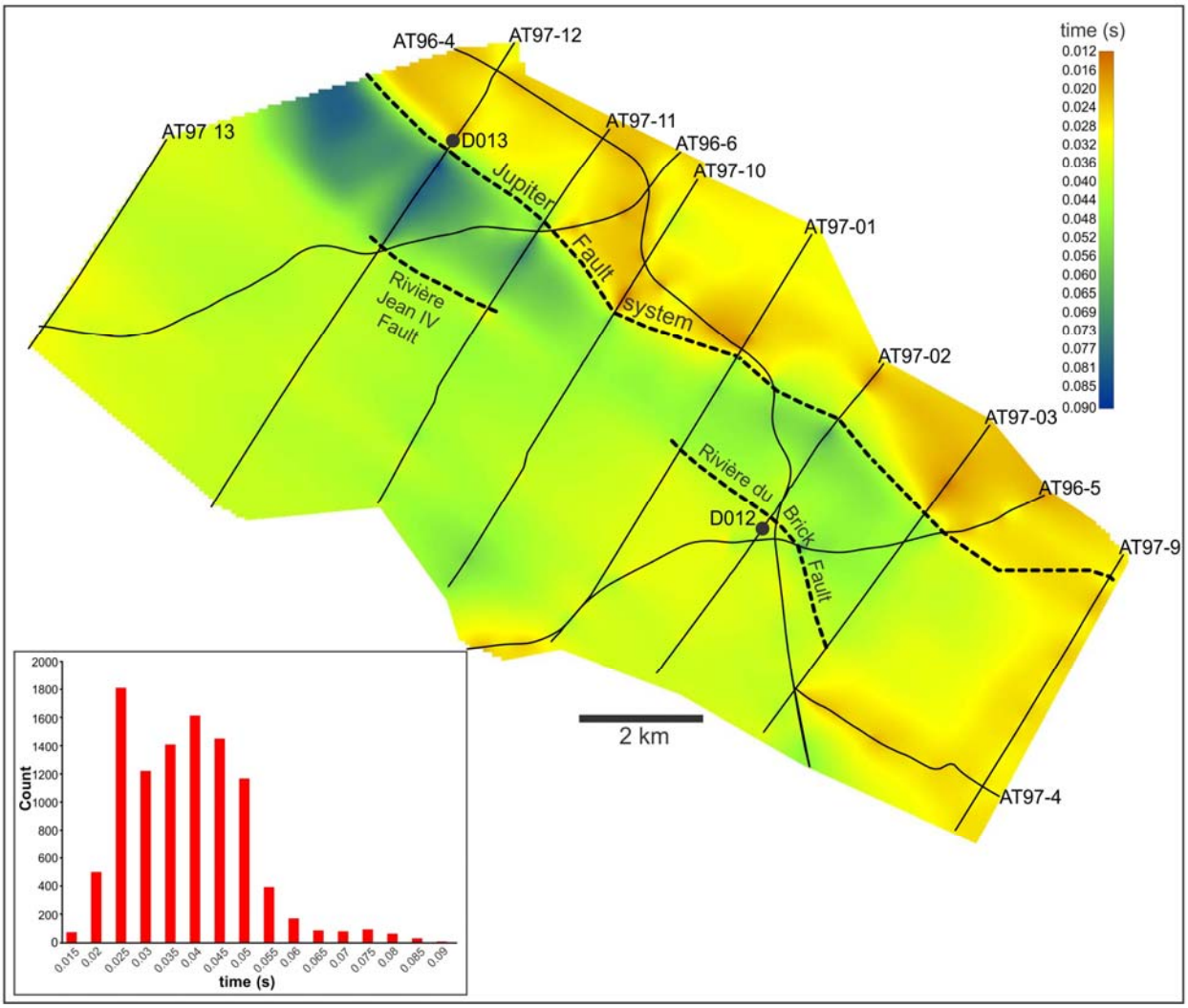

APPENDIX 2.

Interval velocity map of the Macasty Formation computed from Dix (1955) method and the gradient projection optimization algorithm (GPOA). Inset shows the distribution of interval velocity estimations.

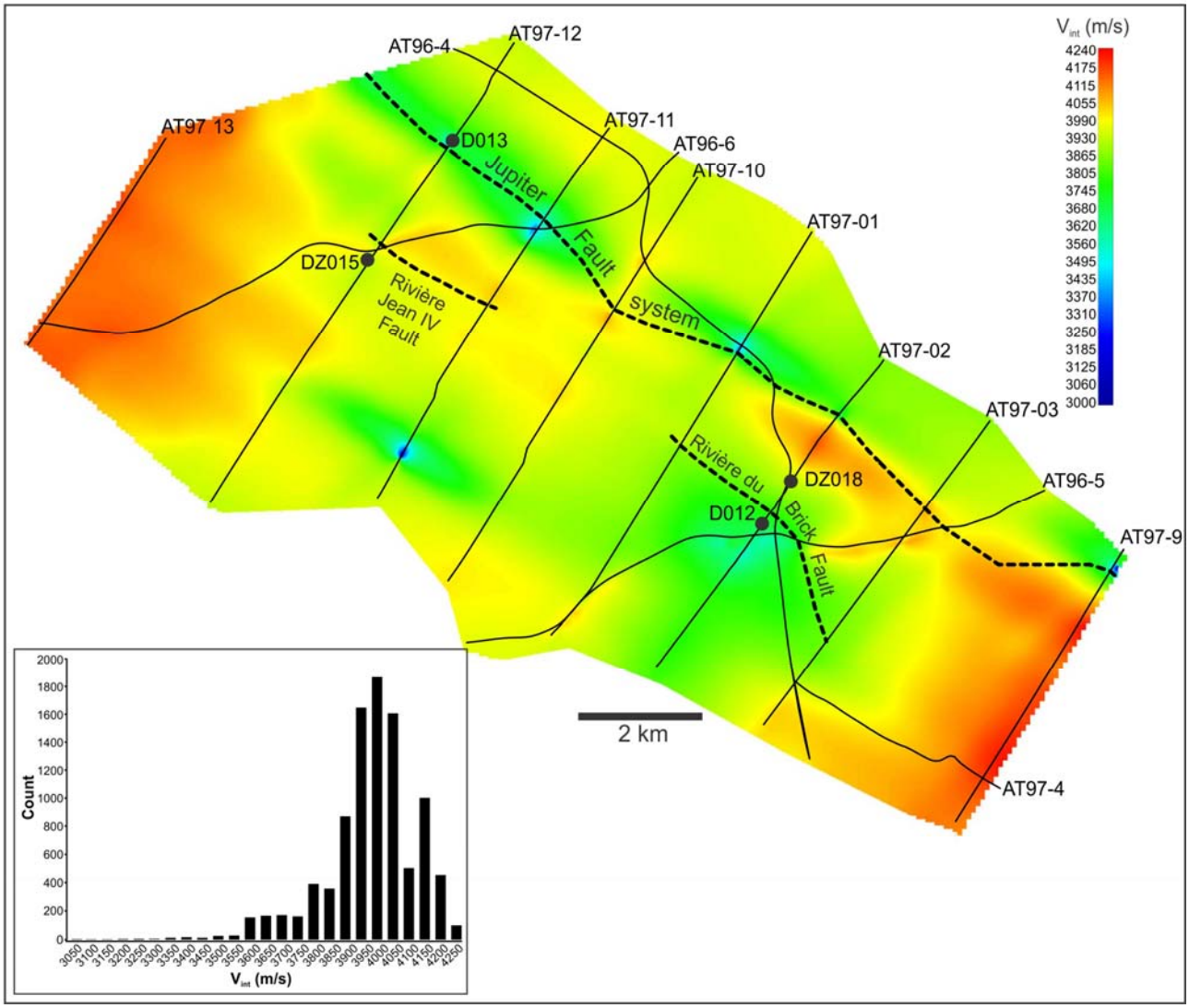

REFERENCES

Achab, A., Asselin, E., Desrochers, A., Riva, J. F., Farley, C., 2011. Chitinozoan biostratigraphy of a new Upper Ordovician stratigraphic framework for Anticosti Island, Canada. Geological Society of America Bulletin, v. 123, p. 186-205.

Bédard, K., Comeau, F.-A., Malo, M., 2014. Lithostratigraphie standardisée et modélisation géologique 3D du bassin d'Anticosti. Rapport R-1561, Institut National de la Recherche Scientifique –Centre Eau-Terre-Environnement, 83p.

Bertrand, R., 1987. Maturation thermique et potentiel pétroligène des séries post-taconiennes du nord-est de la Gaspésie et de l'île d'Anticosti. Doctorate Thesis, Université de Neufchâtel, Suisse, 647 p.

Bordet, E., Malo, M., Kirkwood, D., 2010. A structural study of western Anticosti Island, St. Lawrence platform, Quebec: A fracture analysis that integrates surface and subsurface structural data. Bulletin of Canadian Petroleum Geology, v. 58, p. 36-55.

Brake, V., Pinet, N., 2015. Additional insights on fracture patterns in the northern Anticosti Basin from satellite, aerial and bathymetric images. Geological Survey of Canada, Open File 7911, 21 p.

Castonguay, S., Wilson, R. A., Brisebois, D., Desrochers, A., Malo, M., 2005. Compilation géologique, Anticosti-Gaspé- Campbellton, les ponts géologiques de l'est du Canada, Transect 4, Québec-Nouveau-Brunswick. Commission Géologique du Canada, Open File 4883, 1:125 000, 4 sheets.

Chen, Z., Lavoie, D., Jiang, C., Duchesne, M. J., Malo, M., 2016. Geological characteristics and petroleum resource assessment of the Macasty Formation, Anticosti Island, Quebec, Canada, Geological Survey of Canada Open File 8018, 61 p.

Desrochers, A., 1988. Stratigraphie de l'Ordovicien de la région de l'Archipel de Mingan, Ministère des Ressources Naturelles du Québec, MM 87-01, 62 p.

Desrochers, A., 2006. Rocky shoreline deposits in the Lower Silurian (upper Llandovery, Telychian) Chicotte Formation, Anticosti Island, Quebec. Canadian Journal of Earth Sciences, v. 43, p. 1-10.

Desrochers, A., Farley, C., Achab, A., Asselin, E., Riva, J. F., 2010. A far-field record of the end Ordovician glaciation: The Ellis Bay Formation, Anticosti Island, Eastern Canada, Palaeogeography, Palaeoclimatology, Palaeoecology, v. 296, p. 248-263.

Desrochers, A., Brennan-Alpert, P., Lavoie, D., Chi, G., 2012. Regional stratigraphic, depositional and diagenetic patterns from the interior of the St. Lawrence Platform: the Lower Ordovician Romaine Formation, western Anticosti Basin, Québec. In J.R. Derby, R. D. Fritz, S. A. Longacre, W. A. Morgan, C. A. Sternbach, (eds.) The great American carbonate bank: The geology and economic resources of the Cambrian - Ordovician Sauk megasequence of Laurentia, Memoir of the American Association of Petroleum Geologists, 98, p. 525-543.

Dix, C. H., 1955. Seismic velocities from surface measurements. Geophysics, v. 20, p. 68–86.

Duchesne, M. J., Chen, Z., Lavoie, D. 2016. Seismic imaging of a thin unconventional reservoir in highly attenuating media: the case of the Macasty Formation, Anticosti Island, Canada. Society of Exploration Geophysicists Expanded Abstracts, 4 p.

Fossen, H., Rotevatn, A., 2016. Fault linkage and relay structures in extensional settings- a review. Earth Science Reviews, v. 154, p. 14-28.

Gazdag, J., Sguazzero, P., 1984. Migration of seismic data by phase shift plus interpolation. Geophysics, v. 49, p. 124-131.

Giba, M., Walsh, J. J., Nicolas, A., 2012. Segmentation and growth of an obliquely reactivated normal fault. Journal of Structural Geology, v. 39, p. 253-267.

Jones, I., Levy, S., 1987. Signal-to-noise enhancement in multichannel seismic data via the Karhunen-Loéve Transform. Geophysical Prospecting, v. 35, p. 12-32.

Lavoie, D., Pinet, N., Dietrich, J., Hannigan, P., Castonguay, S., Hamblin, A P., Giles, P., 2009. Petroleum resource assessment, Paleozoic successions of the St. Lawrence Platform and Appalachians of eastern Canada. Geological Survey of Canada, Open File 6174, 273 p.

Lynch, G., 2001. Shell Canada – Encal Energy, Anticosti Island Exploration 1997-2000. Ministère des Ressources Naturelles et de la Faune du Québec, Report 2000TD456-01, 32 p.

Matheney, M. P., Nowack, R. L., 1995. Seismic attenuation values obtained from instantaneous-frequency matching and spectral ratios. Geophysical Journal International, v. 123, p. 1-15.

Pinet. N., Brake, V, Lavoie, D., 2015. Geometry and regional significance of joint sets in the Ordovician-Silurian Anticosti Basin: new insights from fracture mapping. Geological Survey of Canada, Open File 7752, 26 p.

Richardson, J., 1857. Report for the year 1856, of Mr. James Richardson, explorer, addressed to Sir William E. Logan, provincial geologist. In W. E. Logan (ed.) Report of progress for the years 1853-54-55-56, Geological Survey of Canada, p. 191-245.

Rotevatn, A., Bastesen, E., 2014. Fault linkage and damage zone architecture in tight carbonate rocks in the Suez Rift (Egypt): implication for permeability structure along segmented normal faults. In Spence, G. H., Redfern, J., Aguilera, R., Bevan, T. G., Grosgrove, J.W., Couples, G. D., Daniel, J-M. (eds), Advance in the study of fractured reservoirs. Geological Society of London, Special publication 374, p. 79-95.

Rosen, J. B., 1960. The gradient projection method for nonlinear programming. Part I. Linear constraints. Journal of the Society for Industrial and Applied Mathematics, v.8, p.181-217.

Rosen, J. B., 1961. The gradient projection method for nonlinear programming. Part II. Nonlinear constraints. Journal of the Society for Industrial and Applied Mathematics, v.9, p. 514-532.

Sami, T., Desrochers, A. 1992. Episodic sedimentation on an early Silurian, storm-dominated carbonate ramp, Becscie and Merrimack formations, Anticosti Island, Canada. Sedimentology, v. 39, p. 355-381.

Schuchert, C., Twenhofel, W. H. 1910. Ordovicic-Siluric section of the Mingan and Anticosti Islands, Gulf of Saint Lawrence. Bulletin of the Geological Society of America, v. 21, p. 677-716.

Séjourné, S., 2015a. Étude géomécanique de la Formation de Macasty et de sa couverture dans un puits pétrolier et gazier (Pétrolia/Corridor Chaloupe No. 1), Île d'Anticosti, Québec. Commission géologique du Canada, Dossier Public 7892, 52p.

Séjourné, S., 2015b. Étude géomécanique régionale de la Formation de Macasty et de sa couverture d'après les puits pétroliers et gaziers de l'Île d'Anticosti, Québec. Commission géologique du Canada, Dossier public 7907, 114 p.

Sheriff, R. E., Geldart, L. P., 1995. Exploration Seismology. Cambridge University Press, New York, 592 p.

Sloss, L. L., 1963. Sequences in the cratonic interior of North America. Geological Society of America Bulletin, v. 74, p. 93–114.

Twenhofel, W. H., 1927. Geology of Anticosti Island. Memoir 154, Geological Series no. 135, 481 p.

Williams, M. Jenner, E., 2002. Interpreting seismic data in the presence of azimuthal anisotropy; or azimuthal anisotropy in the presence of the seismic interpretation. The Leading Edge, v.21, p.771-774.